Electrochimica Acta 53 (2008) 7599–7613

Contents lists available at ScienceDirect

Electrochimica Acta

journal homepage: www.elsevier.com/locate/electacta

Intercalation dynamics in rechargeable battery materials: General theory and phase-transformation waves in $LiFePO_4$

Gogi K. Singh [a], Gerbrand Ceder [b], Martin Z. Bazant [a,c,*]

[a] Department of Mathematics, Massachusetts Institute of Technology, Cambridge, MA 02139, USA
[b] Department of Materials Science and Engineering, Massachusetts Institute of Technology, Cambridge, MA 02139, USA
[c] Physico-Chimie Théorique, Gulliver-CNRS, ESPCI, 10 rue Vauquelin, Paris 75005, France

ARTICLE INFO

Article history:
Received 27 January 2008
Received in revised form 30 March 2008
Accepted 30 March 2008
Available online 14 April 2008

Keywords:
Rechargeable battery
Intercalation
Phase transformation
Nonlinear waves, Phase-field model,
$LiFePO_4$

ABSTRACT

A general continuum theory is developed for ion intercalation dynamics in a single crystal of rechargeable-battery composite electrode material. It is based on an existing phase-field formulation of the bulk free energy and incorporates two crucial effects: (i) anisotropic ionic mobility in the crystal and (ii) surface reactions governing the flux of ions across the electrode/electrolyte interface, depending on the local free energy difference. Although the phase boundary can form a classical diffusive "shrinking core" when the dynamics is bulk-transport-limited, the theory also predicts a new regime of surface-reaction-limited (SRL) dynamics, where the phase boundary extends from surface to surface along planes of fast ionic diffusion, consistent with recent experiments on $LiFePO_4$. In the SRL regime, the theory produces a fundamentally new equation for phase transformation dynamics, which admits traveling-wave solutions. Rather than forming a shrinking core of untransformed material, the phase boundary advances by filling (or emptying) successive channels of fast diffusion in the crystal. By considering the random nucleation of SRL phase-transformation waves, the theory predicts a very different picture of charge/discharge dynamics from the classical diffusion-limited model, which could affect the interpretation of experimental data for $LiFePO_4$.

1. Introduction

$LiFePO_4$ is widely considered to be a promising cathode material for high-rate Li-ion rechargeable batteries, so it provides a natural setting to develop mathematical models of charge/discharge dynamics. The high practical capacity and reasonable operating voltage of the material, along with its nontoxicity and potential low cost, make it well-suited for large-scale battery applications [1–3]. Unlike many other cathode materials that increase their Li concentration in a continuous solid solution, Li_xFePO_4 only exists for $x \approx 0$ and $x \approx 1$ [4] and charges or discharges with Li by changing the fraction of phase with $x \approx 0$ and $x \approx 1$. This tendency for phase separation, coupled with strong crystal anisotropy, poses significant challenges for any attempt to describe intercalation dynamics with continuum models, which until now have been limited to isotropic "shrinking-core" models [5,6].

In contrast to the simplicity of current continuum models, rather complex phase-transformation and transport properties have been revealed by atomistic simulations [7–10]. For example, first-principles calculations have shown that Li diffusion in the bulk $FePO_4$ crystal is highly anisotropic [7,8]. Li is essentially constrained to 1D channels in the (0 1 0) direction, as depicted in Fig. 1. The lattice mismatch at the $FePO_4/LiFePO_4$ phase boundary is significant (5% in the x direction, shown in Fig. 1), and recent work has investigated the differences in elastic properties between the lithiated and unlithiated material [11]. Atomistic simulations have also suggested that electrons in the crystal may diffuse as small, localized polarons confined to planes parallel to the Li channels [12–14].

Recent experiments have confirmed the anisotropic transport and phase separation of Li in single crystal $LiFePO_4$ [15–17]. Moreover, detailed microscopy in these studies has revealed that the $FePO_4/LiFePO_4$ phase boundary is a well-defined interface that extends through the bulk crystal to the surface. In experiments, the phase boundary has a characteristic width of several nanometers on the surface [16], although this width is probably broadened by experimental resolution, and Li insertion and extraction seem to be concentrated in this region, with negligible transfer occurring in either the $FePO_4$ or $LiFePO_4$ phases. Notably, the phase boundary moves orthogonally to the direction of the surface flux, indicating that as Li insertion (extraction) proceeds, layers of the 1D channels are progressively filled (emptied). The observation of surface cracks and their alignment with the phase boundary [15] also reinforces

* Corresponding author.
E-mail address: bazant@math.mit.edu (M.Z. Bazant).

0013-4686/$ – see front matter © 2008 Elsevier Ltd. All rights reserved.
doi:10.1016/j.electacta.2008.03.083

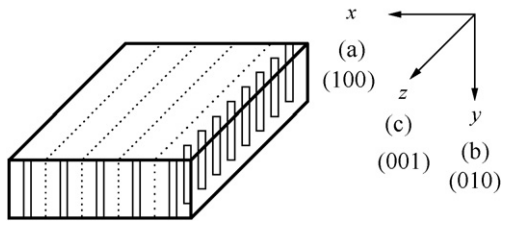

Fig. 1. Schematic of plate-like single crystals of $LiFePO_4$. Li is confined to 1D channels in the *y* direction, and channels are stacked in layers parallel to the *yz*plane, indicated by the dotted lines. Typical dimensions of single crystals are 2 μm × 0.2 μm × 4 μm in the *x*, *y*, *z* dimensions, respectively [15]. For each direction, the corresponding space group *Pnma* axis and Miller index are shown in parentheses.

the view that the $FePO_4/LiFePO_4$ lattice mismatch plays an important role in the electrochemical function of the material, as may the associated stress field [18].

In light of the understanding gained from these atomistic and experimental studies, the continuum theory of transport and phase separation in $LiFePO_4$merits renewed attention. The prevailing shrinking-core model can be traced to a qualitative picture accompanying the first experimental demonstration of the material as an intercalation electrode [1]. This model assumes a growing shell of one phase surrounding a shrinking core of the other phase, with the shell and core phases determined by the direction of the net Li flux: a $LiFePO_4$shell surrounds an $FePO_4$core during Li insertion (battery discharging); an $FePO_4$ shell surrounds a $LiFePO_4$ core during Li extraction (battery charging). It is important to note that in such a model the boundary between the shell and core phases is entirely contained within the bulk of the material and moves parallel to the direction of the Li flux, in contrast to the observations of the experiments cited above.

The current state of mathematical modeling of ion intercalation is based on the shrinking-core concept with some further simplifying assumptions. In earlier work, a simplified version of the model was mathematically formulated by Srinivasan and Newman [5] and incorporated into an existing theory for transport in composite cathodes [6]. In their model, $FePO_4$is treated as a continuous, isotropic material, and Li is inserted and extracted uniformly over the surface of a spherical $FePO_4$particle. The phase boundary is defined as where the compositions $Li_\epsilon FePO_4/Li_{1-\epsilon}FePO_4$ coexist, with $\epsilon \ll 1$ specifying the equilibrium composition between the Li-poor and Li-rich phases, and no nucleation constraints are included. Only Li transport in the shell is considered and modeled by an isotropic, constant diffusivity diffusion equation, while the velocity of the phase boundary is prescribed by a mass balance across the boundary. Thus, for Li insertion (extraction), diffusion in the growing shell occurs between the surface Li concentration and $1-\epsilon$ (ϵ). The value of ϵ is set as a parameter in the numerical solution of the model.

In this paper, we develop a continuum theory for ionic transport and phase separation in single-crystal rechargeable battery materials, motivated by the special case of $LiFePO_4$, but also more generally applicable. Our theory accounts for anisotropic ionic diffusion in the bulk as well as the formation and dynamics of a localized phase boundary, driven by surface reactions at the electrolyte/electrode interface. We utilize an existing phase-field model for the free energy of the system, which has been used to calculate the Li chemical potential in $FePO_4$[19]; the bulk transport equation and surface reaction rates for Li are then derived in terms of this chemical potential. The phase-field approach provides a sound thermodynamic basis for studying the system and also directly connects our theory to first-principles atomistic modeling, which can accurately compute chemical potentials in a wide range of intercalation compounds [20,21].

In this initial effort, we neglect the possibility of charge separation and assume that electrons are freely available in the material to compensate ionic charges; the presence of multiple diffusing and migrating charged species (interacting through an electrostatic potential) can be modeled as an extension of the general framework we present. We also avoid an explicit treatment of stresses generated by mismatch strain across the phase boundary, which could play an important role in some processes. Instead, we indicate how elastic energy could be added to the model and note that a term in the phase-field formulation may serve as a local approximation of the lattice-mismatch energy. In any case, we will see that this simple approach already suffices to explain some of unusual features of phase-transformation dynamics in $LiFePO_4$.

The paper is organized as follows. In Section 2, we begin by developing a general model for intercalation dynamics, notably taking into account crystal anisotropy and the tendency for phase separation, as well as composition dependence of surface reactions. That section concludes with a discussion of possible regimes of phase-transformation dynamics in strongly phase separating materials, including a new regime of surface-reaction-limited (SRL) dynamics, where the flux is concentrated at a phase boundary that extends to the surface along channels of fast bulk diffusion. The SRL regime, which has obvious relevance for $LiFePO_4$, is analyzed in detail in Section 3, where a reduced depth-integrated model is derived and shown to have wave solutions, which are characterized in detail. The fundamental implications of SRL phase-transformation waves for current–voltage measurements are discussed in Section 4, and we close with some general conclusions.

2. General mathematical model

In this section, we present a general continuum framework to describe intercalation dynamics in rechargeable battery materials. In principle, our model can be adapted to arbitrary intercalation compounds, not only phase separating systems, such as $FePO_4/LiFePO_4$, but also materials forming solid solutions, such as Li_xCoO_2, depending on the parameters. For a given material, depending on the chemical driving force and physical constants, there can be different modes of phase-transformation dynamics. In the next section, we will focus on a new dynamical mode limited by surface reactions in a strongly anisotropic crystal, which clearly could not be described by existing isotropic models.

2.1. Phase-field formulation

We follow the conventional Cahn–Hilliard phase-field model [22] applied to an anisotropic intercalation compound, where the total free energy of the system is expressed as a functional of the local ionic concentration

$$F = \int \left[\bar{f}(c) + \frac{1}{2}\nabla c \cdot \mathbf{K}\nabla c \right] \mathrm{d}\mathbf{r}, \tag{1}$$

where c is the dimensionless, normalized concentration ($0 < c < 1$), $\bar{f}(c)$ the homogeneous free energy density, and $\mathbf{K}$ is a symmetric, positive definite tensor that represents the energy penalties for maintaining concentration gradients of different orientations in the system. An isotropic version of this phase-field model with $K_{ij} = K\delta_{ij}$ (where δ_{ij} is the Kronecker delta function, or identity matrix) has previously been developed for bulk transport in $LiFePO_4$ with $\bar{f}(c)$ fitted to atomistic simulations [19], although in this section we

envision more general applications. (For a recent review of phase-transformation modeling in solids, see Ref. [23].)

In strongly phase separating systems, the phase boundary usually coincides with the concentration gradient, so the gradient penalty in (1) can be regarded as approximating related contributions to the free energy. Phase-field models have also been developed, which include long-range elastic contributions to the free energy [24,25], but here we restrict ourselves to the simpler formulation above in order to focus on other effects, namely anisotropic transport and surface reactions. In this spirit, we also ignore any surface contributions to the free energy, such as the tension of the electrode/electrolyte interface.

In the simplest continuum approximation of intercalation into a crystal lattice, the homogeneous, bulk free energy density takes the form of a regular solution model

$$\bar{f}(c) = ac(1-c) + \rho kT\left[c\ln c + (1-c)\ln(1-c)\right], \tag{2}$$

where a is the average energy density (in a mean field sense) of the interaction between Li ions, ρ the number of intercalation sites per unit volume, k the Boltzmann's constant, and T is the temperature. The first term in (2), the enthalpic contribution to the free energy, promotes separation of the system to $c = 0$ or 1, while the second term, the entropic contribution, favors mixing of the system. Therefore, the strength of the phase separation is characterized by the dimensionless ratio $a/\rho kT$.

The chemical potential of an ion in the host crystal is calculated as a variational derivative of the free energy

$$\mu = \frac{\delta F}{\delta c} = \bar{\mu} - \nabla\cdot\mathbf{K}\nabla c, \tag{3}$$

where we define $\bar{\mu}$ as the homogeneous chemical potential

$$\bar{\mu} = \frac{\partial \bar{f}}{\partial c} = a(1-2c) + \rho kT\ln\left(\frac{c}{1-c}\right). \tag{4}$$

While in general, the two phase compositions in equilibrium across the miscibility gap are determined by the common tangent construction, in the symmetric free energy $\bar{f}$ of (2) these compositions correspond to $\bar{\mu} = 0$. These roots cannot be found analytically from (4), but asymptotic approximations in the small parameter $\rho kT/a$ can be obtained; two term expansions are

$$c_- \sim \mathrm{e}^{-a/\rho kT}\left(1 + \frac{a}{\rho kT}\mathrm{e}^{-a/\rho kT}\right), \tag{5}$$

$$c_+ \sim 1 - c_-, \tag{6}$$

where c_- is the root near $c = 0$ and c_+ is the root near $c = 1$. As may be expected, $c_\pm$ approach the concentration extremes exponentially in $a/(\rho kT)$. While nucleation may be required to form a second phase for compositions in the miscibility gap, spontaneous phase separation occurs when the composition is within the spinodals. The spinodals correspond to the zeros of the curvature of the free energy and can be determined from (2) as

$$c_{\mathrm{sp}} = \frac{1 \pm \sqrt{1 - 2\rho kT/a}}{2}. \tag{7}$$

We observe that $a > 2\rho kT$ is required for distinct, physically meaningful spinodal compositions.

2.2. Anisotropic bulk transport

Intercalation compounds typically have anisotropic layered crystal structures, where ions diffuse much more easily in certain directions than others. In standard transition-metal (M) oxide materials of the form Li_xMO_2, ions tend to move more freely between oxide layers than in the transverse direction [26]. The mobility of Li in $FePO_4$is even more complicated. As described above, Li migration in the bulk crystal is confined to 1D channels in the (0 1 0) direction, labeled as y in Fig. 2. Some diffusion in other directions may occur due to defects in the crystal lattice or cracks caused by the $FePO_4$/$LiFePO_4$lattice mismatch, as have been observed experimentally [15,16]. Experiments [15,16] have found that layers of stacked 1D channels in the z direction are progressively filled or emptied as the phase boundary moves across the layers in the x direction, indicating that transport in the z direction is faster than transport in the x direction.

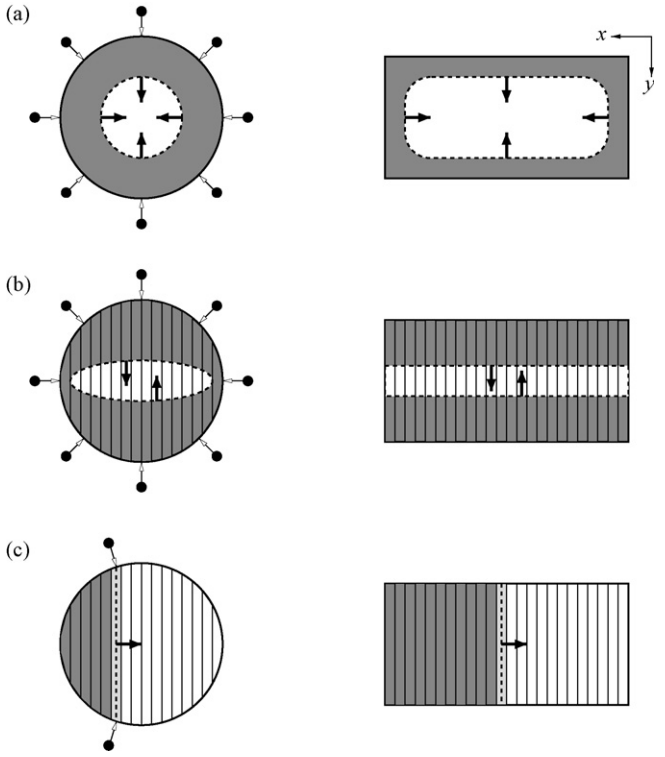

Fig. 2. Transport models obtained in different limits of the characteristic timescales for bulk diffusion and surface reactions. Figures show xy cross sections of spherical and plate-like single crystals during Li insertion, after phase nucleation has occurred. Lithiated portions of the crystal are shaded, and points outside particles represent flux of Li ions across the electrode/electrolyte interface (shown only for spherical particles). The $FePO_4$/$LiFePO_4$ phase boundary is denoted by the dashed line, and arrows indicate movement of the boundary as insertion proceeds. (a) Isotropic bulk transport limited. (b) Anisotropic bulk transport limited. (c) Anisotropic surface reaction limited.

In general, therefore, we must postulate a tensorial relation for the ionic flux

$$\mathbf{j} = -c\mathbf{B}\nabla\mu, \tag{8}$$

where we make the standard approximation of linear response to chemical potential gradients with a symmetric, positive definite mobility tensor $\mathbf{B}$. In the common case of an orthorhombic crystal, this tensor is diagonal, $B_{ij} = b_{ii}\delta_{ij}$, but it is generally not isotropic. For example, we have $b_{11} \ll b_{33} \ll b_{22}$ for Li in $FePO_4$, where the indices 1, 2, 3 correspond to the x, y, z directions, respectively, defined in Fig. 1. In commonly used intercalation oxides, such as CoO_2(which has hexagonal crystal structure), the mobility of Li in any direction confined between oxide layers is likewise much greater than in any out-of-plane direction.

With the ionic fluxes thus defined, the dynamics of the concentration profile is governed by the mass conservation law

$$\rho\frac{\partial c}{\partial t} + \nabla\cdot\mathbf{j} = 0, \tag{9}$$

where the factor of ρ (density of intercalation sites) is needed for dimensional consistency.

The diffusivity tensor is determined from the mobility tensor by the Einstein relation $\mathbf{D} = kT\mathbf{B}$. Note that $\mathbf{D}$ can, in general, depend on position or concentration. Even if it is constant, the phase-field formulation of the flux density (8) implies a concentration-dependent *chemical diffusivity*,

$$\mathbf{D}^{\text{chem}}(c) = \mathbf{B}\frac{c}{\rho}\frac{\mathrm{d}\bar{\mu}}{\mathrm{d}c} = \mathbf{D}\left(1 - \frac{2ac}{\rho kT} + \frac{c}{1-c}\right) \tag{10}$$

which would enter into a nonlinear generalization of Fick's Law, $\mathbf{j} = -\mathbf{D}^{\text{chem}}\rho\nabla c$ in the limit of negligible gradient penalty ($|\nabla\cdot\mathbf{K}\nabla c| \ll |\bar{\mu}|$). In this case, our use of the regular solution model (2) leads to two concentration-dependent terms in (10): the first, enthalpic term promoting phase separation and the second, entropic term enforcing volume constraints. For the solid-solution compound Li_xCoO_2, first principles calculations have shown that the chemical diffusivity is a highly nonlinear function of the Li concentration, varying by several orders of magnitude over the composition range [26]. Such effects can be less dramatic in strongly phase separating materials, at least in the model. Even with the non-Fickian flux from the gradient penalty term in (8), numerical solutions of the same model applied to $LiFePO_4$have shown that both potentiostatic and galvanostatic response can be reasonably approximated by an effective Fickian diffusion coefficient D^{eff}.

2.3. Surface reactions

We assume that Arrhenius kinetics govern the insertion and extraction rates of ions across the electrode/electrolyte interface, where the activation energies are related to the difference in *chemical potential* of ions across the interface, which provides the thermodynamic driving force. In standard models of electrochemical charge-transfer reactions, such as the Butler–Volmer equation [27,28], activation energies depend only on the difference in electrostatic potential, and concentration-dependent chemical interactions of ions with other molecules in the two phases are neglected. In our model, the overpotential biasing the reactions could be explicitly described by adding electrostatic energy to the chemical potentials, but here we choose to focus instead on novel effects of compositional changes in the crystal on the local reaction rate.

For simplicity, we assume that the chemical potential of ions in the host crystal, μ in Eq. (3), is valid everywhere on the electrode surface where transfer reactions occur, (crucially) including the gradient penalty term. By also using the bulk chemical potential for ions at the crystal surface, we are neglecting the possibility of any variation in the chemical potential at the electrode/electrolyte interface, e.g. due to surface orientation or surface curvature, as noted above [29]. In reality, electron-transfer reactions must also occur at the intersection of three phases—the host crystal in contact with composite matrix containing the electrolyte and an electron-conducting phase, whose local structure we also neglect in our simplified treatment.

With these assumptions, we postulate the following form for the insertion rate density of ions into the host crystal

$$R_{\text{ins}} = k_{\text{ins}} c_{\text{e}}\, \mathrm{e}^{(\mu_{\text{e}}-\mu)/(\rho kT)}, \tag{11}$$

where k_{ins} is the insertion rate coefficient, and c_{e} and μ_{e} are the concentration and chemical potential of Li in the electrolyte, respectively. Note that since c_{e} is expressed as a dimensionless filling fraction, R_{ins} and k_{ins} have dimensions of inverse time. In alternate formulations of the model, different forms for the reaction rate could be assumed (see below), but the key feature for our predictions below is the Arrhenius dependence on the chemical potential of intercalated ions in the crystal, given by the phase-field model above.

In a more complete battery model, c_{e} and μ_{e} would be determined by solving the appropriate transport equations for ions in the electrolyte, as well as possibly electrons in the conducting phase. However, since we focus here on ion transport in the intercalation compound, we ignore variations in the electrolyte and take c_{e} and μ_{e} to be constants. Our formulation therefore describes potentiostatic, or constant chemical equilibrium, conditions in the electrolyte, with the interfacial transfer of ions as the rate limiting process. Absorbing the (dimensionless) constant c_{e} into k_{ins} then gives

$$R_{\text{ins}} = k_{\text{ins}}\, \mathrm{e}^{\beta(\mu_{\text{e}}-\mu)} = \bar{R}_{\text{ins}}\, \mathrm{e}^{\beta\nabla\cdot\mathbf{K}\nabla c}, \tag{12}$$

where $\beta = 1/(\rho kT)$ and $\bar{R}_{\text{ins}}$ is the homogeneous insertion rate

$$\bar{R}_{\text{ins}} = k_{\text{ins}}\left(\frac{1-c}{c}\right)\mathrm{e}^{\beta[\mu_{\text{e}}-a(1-2c)]}. \tag{13}$$

Similarly, the extraction rate is assumed to have the form

$$R_{\text{ext}} = k_{\text{ext}} c\, \mathrm{e}^{\beta(\mu-\mu_{\text{e}})} = \bar{R}_{\text{ext}}\, \mathrm{e}^{-\beta\nabla\cdot\mathbf{K}\nabla c}, \tag{14}$$

where $\bar{R}_{\text{ext}}$ is the homogeneous extraction rate

$$\bar{R}_{\text{ext}} = k_{\text{ext}}\left(\frac{c^2}{1-c}\right)\mathrm{e}^{\beta[a(1-2c)-\mu_{\text{e}}]}. \tag{15}$$

Finally, the net rate of insertion is

$$R = R_{\text{ins}} - R_{\text{ext}} = \bar{R}_{\text{ins}}\, \mathrm{e}^{\beta\nabla\cdot\mathbf{K}\nabla c} - \bar{R}_{\text{ext}}\, \mathrm{e}^{-\beta\nabla\cdot\mathbf{K}\nabla c}, \tag{16}$$

$$R = k_{\text{ins}}\left(\frac{1-c}{c}\right)\mathrm{e}^{\beta[\mu_{\text{e}}-a(1-2c)+\nabla\cdot\mathbf{K}\nabla c]} - k_{\text{ext}}\left(\frac{c^2}{1-c}\right)\mathrm{e}^{\beta[a(1-2c)-\mu_{\text{e}}-\nabla\cdot\mathbf{K}\nabla c]}. \tag{17}$$

Note that in this formulation there is broken symmetry about $c = 1/2$ in the net reaction rate.

The boundary conditions for (9) on the crystal surface express mass conservation at the electrode/electrolyte interface,

$$\mathbf{n}\cdot\mathbf{j} = -\rho_{\text{s}} R, \tag{18}$$

where $\mathbf{n}$ is the unit normal vector directed out of the crystal, and ρ_{s} is the number of intercalation sites per unit area, which depends on the orientation of the surface. Consistent with our neglect of surface excess chemical potential, we neglect the possibility of a surface flux density $\mathbf{j}_{\text{s}}$, whose surface divergence $\nabla_{\text{s}}\cdot\mathbf{j}_{\text{s}}$ would appear as an extra term on the right hand side of (18).

Before continuing, it is worth emphasizing the unusual compositional dependence of these expressions. We are not aware of any prior model of chemical reaction kinetics (not only in electrochemistry) where *concentration gradients contribute to the activation energy*. This will turn out to be an essential ingredient for our prediction of phase-transformation waves transverse to the lithium flux in the following sections. Here such novel terms arise via the gradient penalty in the chemical potential from a phase-field model used on one side of the reaction interface.

As long as this crucial feature is maintained, we expect the qualitative predictions below to be robust for a variety of different models for the reaction rate. Here, we adopt Eq. (16) simply as an example in this class, which leads to new modes of intercalation dynamics. Alternate forms for the reaction rate can be derived systematically from transition rate theory, assuming thermal activation over a chemical potential energy barrier [30]. For example, if we define excess chemical potentials, $\mu^{\text{ex}} = \mu - \rho kT\log c$ and $\mu_{\text{e}}^{\text{ex}} = \mu_{\text{e}} - \rho kT\log c_e$, and shift the barrier in proportion to the

thermodynamic driving force, $\Delta\mu^{ex} = \mu_e^{ex} - \mu^{ex}$, then the net insertion rate is

$$R = R_{ins} - R_{ext} = k_0 \left(c_e \, e^{\alpha_{ins}\beta\,\Delta\mu^{ex}} - c \, e^{-\alpha_{ext}\beta\,\Delta\mu^{ex}} \right) \quad (19)$$

where k_0 is a rate constant and α_{ins} and α_{ext} are (positive) transfer coefficients, analogous to those standard models for electrochemical reactions [28], where $\Delta\mu$ is simply a voltage difference, without any compositional dependence. In contrast, in Eq. (16) we have arbitrarily replaced $\Delta\mu^{ex}$ with $\Delta\mu = \mu_e - \mu$ and set $\alpha_{ins} = \alpha_{ext} = 1$ to avoid introducing additional parameters, but this modifies the concentration dependence of $\bar{R}_{ins}$ and $\bar{R}_{ext}$. In the context of transition rate theory, one would instead require $\alpha_{ins} + \alpha_{ext} = 1$ to satisfy de Donder's relation, $R_{ins}/R_{ext} = e^{\beta\Delta\mu}$, and different models of the activation free energy could also be postulated. Exploring such modifications of the reaction rate on phase-transformation dynamics in our theory is a subject of current work in our group, beyond the scope of this paper.

2.4. Fundamental regimes of phase-transformation dynamics

The general model from the preceding sections describes a reaction-diffusion system with a composition-dependent reaction rate R and an anisotropic chemical diffusivity $\mathbf{D}^{chem}$. For strongly phase-separating systems (our primary interest here), we can make some simple scaling arguments to try to anticipate its basic dynamical regimes, sketched in Fig. 2. For the purpose of these crude estimates, we ignore composition dependence of the reaction rate, except to note that it is focused on regions of varying composition by the gradient term. Motivated by the simulations of Han et al. [19] with the same bulk phase-field model, we assign a constant effective Fickian diffusivity D_i^{eff} to each coordinate direction ($i = x, y, z$), along which the crystal has a typical length scale L_i and reaction rate R_i.

With these gross simplifications, in a given direction i, the characteristic timescales for bulk diffusion and surface reactions are

$$t_i^D = \frac{L_i^2}{D_i^{eff}} \quad \text{and} \quad t_i^R = \frac{1}{R_i}, \quad (20)$$

respectively. The dimensionless ratio of these timescales is a Damkohler number

$$Da_i = \frac{t_i^D}{t_i^R} = \frac{R_i L_i^2}{D_i^{eff}}. \quad (21)$$

An isotropic *bulk-transport-limited* (BTL) process, where bulk diffusion in all directions is much slower than surface reactions, is characterized by

$$Da_x = Da_y = Da_z \gg 1. \quad (22)$$

In this regime, the phase boundary is entirely contained within the material and moves along the direction of the ionic flux, as shown in Fig. 2 a. In the special case of a spherical phase boundary in a spherical, isotropic crystal, the phase boundary ressembles a shrinking core [5].

Anisotropic BTL phase transformation dynamics involves much faster diffusion in one or more crystal directions, while still slower than surface reactions. For example, in layered intercalation compounds, such as $LiCoO_2$, diffusion is much faster between oxide planes in parallel directions than in the perpendicular direction across those planes. The case of fast one-dimensional diffusion channels, examplified by $LiFePO_4$, is depicted in Fig. 2 b. Here, diffusion in the x and z directions is negligible, while diffusion in the more accessible y direction is much slower than surface reactions:

$$Da_x, Da_z \gg Da_y \gg 1, \quad (23)$$

In this regime, the phase boundary still ressembles a shrinking core in the bulk, but ions are confined to 1D channels in the y direction. Here, anisotropy alters the shape of the phase interface, but not its basic diffusive dynamics.

In classical reaction-diffusion models, these dynamical regimes are contrasted with *isotropic surface-reaction-limited* processes, where surface reactions are slower than bulk transport in all directions:

$$Da_x, Da_y, Da_z \ll 1 \quad (24)$$

In this regime, bulk transport is fast enough equilibrate the concentration to a nearly constant value $c(t)$ across the material, which varies uniformly at the slowest reaction time scale. (This case of spatially homogeneous dynamics is not shown in the figure.)

Motivated by the experiments and simulations of $LiFePO_4$ described above, we focus on a new dynamical regime where surface reactions are much slower than diffusion in the y direction but much faster than diffusion in the x and z directions. Thus, we study the limit

$$Da_x, Da_z \gg 1 \gg Da_y, \quad (25)$$

illustrated in Fig. 2 c. The phase boundary in this regime extends through the bulk of the material to the xzsurfaces, and thus allows the dominant reaction-rate R_y to be focused there by the gradient-penalty term. The phase boundary then moves in such a way that each channel is almost completely lithiated (delithiated) before insertion (extraction) progresses to an adjacent channel. For such an *anisotropic surface-reaction-limited* process, our general model reduces to a fundamentally new, depth-averaged equation governing the transport and phase separation dynamics. The reduced model predicts phase transformation by nonlinear wave propagation, rather than a classical diffusive process.

Before analyzing this behavior in the next section, we stress that transitions between the different dynamical regimes in our general model can be induced by changing the applied potential, the size and shape of the crystal and/or the diffusivities (e.g. by the formation of crystal defects [31]). For example, the SRL wave dynamics is expected to breakdown and give way to a BTL regime if the depth L_y of the crystal becomes large enough or D_y^{eff} becomes small enough that $Da_y > 1$. A similar transition occurs if the strength of the driving electrochemical potential $|\mu_e|$ is increased, due to enhanced reaction rates, R_i.

Of course, these reaction-diffusion arguments are oversimplified and only give a sense of possible dynamical regimes in the general model. For example, the reaction rates R_i, and thus the reaction times t_i^R, are non-uniform in time and space and depend on the evolving concentration profile in all regimes. The reaction rates also depend on other physical parameters, such as the gradient penalty tensor K_{ij} and phase-separation energy a. The same parameters affect bulk transport by introducing nonlinear concentration dependence, as noted above. There may also be subtle differences between potentiostatic and galvanostatic response [19]. A detailed parametric study of dynamical transitions in our model is beyond the scope of this paper and will be the subject of future work.

3. Surface-reaction-limited phase-transformation waves

3.1. Depth-integrated model

We now develop a special limit of the general model that describes SRL phase-transformation dynamics, which is relevant for strongly anisotropic phase-separating systems such as $LiFePO_4/FePO_4$. We assume that fast diffusion in the y oriented 1D channels rapidly equilibrates the bulk Li concentration to the

surface concentration. A depth-averaged concentration $\bar{c}$ on the xz surface can therefore be defined as

$$\bar{c} = \frac{1}{L_y(x,z)} \int c(x,y,z,t)\,\mathrm{d}y, \tag{26}$$

where $L_y(x,z)$ is the depth of the crystal in the y direction, from surface to surface.

By depth-averaging the bulk transport Eq. (9), using the boundary condition (18), we find that the dynamics of $\bar{c}$ are governed solely by the surface reaction rate R, acting as a source term on the xzsurface,

$$\left(\frac{\rho L_y(x,z)}{2\rho_s(x,z)}\right)\frac{\partial \bar{c}}{\partial t} = R(\bar{c}, \nabla\cdot\mathbf{K}\nabla\bar{c}), \tag{27}$$

where $\rho_s(x,z)$ is the number of atoms per unit area, dependent on the local orientation of the crystal surface. As noted above, a surface diffusion term could also be explicitly added to (27), but we shall see that the reaction rate R already produces weak xz diffusion due to the gradient penalty, which suffices to propagate the phase boundary along the surface.

Eq. (27) describes a fundamentally different type of phase transformation dynamics. From a mathematical point of view, the striking feature is that the Laplacian term $\nabla^2\bar{c}$ appears in a nonlinear source term, as opposed to the additive quasilinear term in classical reaction-diffusion equations. We are not aware of any prior study of this type of equation, so it begs mathematical analysis to characterize its solutions.

Here, we begin this task by making some simplifying assumptions, which allow us to highlight new nonlinear wave phenomena described by (27). As noted above, experiments indicate that layers of 1D channels along the yz plane are progressively filled or emptied as Li transfer proceeds, so it is natural to neglect concentration variations in the z direction as a first approximation, for a planar phase boundary spanning the crystal. In that case, we only need one component of the gradient penalty tensor in the phase field model, $K_x = K$, in the x direction of wave propagation. We also neglect depth variations, $L_y =$ constant, and assume constant surface orientation, $\rho_s =$ constant, which corresponds to the common case of a plate-like crystal.

3.2. Dimensionless formulation

A dimensionless form of the model, suitable for mathematical analysis, is found by scaling each variable to its natural units. The Li concentration is already expressed as a dimensionless filling fraction per channel $\bar{c}$, which will depend on the dimensionless position $\tilde{x} = x/L$ and time $\tilde{t} = t/\tau$. Position is scaled to a length $L = L_x$, which characterizes the size of the crystal surface along which the SRL phase transformation propagates. The natural time scale from (27) is

$$\tau = \frac{\rho L_y}{2\rho_s k_{\mathrm{ins}}}, \tag{28}$$

which is the time required for the insertion reaction to fill a single fast-diffusion channel in the crystal (from both sides). Note that this time scale is proportional to the depth of the crystal, L_y.

There are four dimensionless groups which govern the solution. The first is the ratio of reaction-rate constants

$$\kappa = \frac{k_{\mathrm{ext}}}{k_{\mathrm{ins}}}, \tag{29}$$

which measures asymmetry in the extraction and insertion reaction kinetics. By scaling energy density to the thermal energy density ρkT, we arrive at three more dimensionless parameters:

$$\tilde{a} = \frac{a}{\rho kT}, \quad \tilde{\mu}_e = \frac{\mu_e}{\rho kT}, \tag{30}$$

and

$$\tilde{\lambda} = \sqrt{\frac{K_x}{\rho kTL^2}} = \frac{\lambda}{L}. \tag{31}$$

The latter formula makes it clear that the natural length scale for the phase boundary thickness, set by the gradient penalty in the free energy, is $\lambda = \sqrt{K_x/(\rho kT)}$. Since λ is an atomic length scale (1 Åto 10 nm) much smaller than the crystal size (10 nm to 10 μm), the parameter $\tilde{\lambda}$ is typically small and lies in the range $10^{-5} < \tilde{\lambda} < 1$.

With these scalings and assuming Eq. (16) for the reaction rate, the SRL phase-transformation Eq. (27) takes the dimensionless form

$$\frac{\partial \bar{c}}{\partial \tilde{t}} = \left(\frac{1-\bar{c}}{\bar{c}}\right)\mathrm{e}^{\tilde{\mu}_e - \tilde{a}(1-2\bar{c}) + \tilde{\lambda}^2(\partial^2\bar{c}/\partial\tilde{x}^2)} - \kappa\left(\frac{\bar{c}^2}{1-\bar{c}}\right)\mathrm{e}^{\tilde{a}(1-2\bar{c}) - \tilde{\mu}_e - \tilde{\lambda}^2(\partial^2\bar{c}/\partial\tilde{x}^2)}, \tag{32}$$

We will study solutions to this new nonlinear partial differential equation in the following sections, but we already can gain some insight by considering the limit of a sharp phase boundary, $\tilde{\lambda} \ll 1$, as discussed above. Expanding (32) for small $\tilde{\lambda}$, we obtain a reaction-diffusion equation at leading order,

$$\frac{\partial \bar{c}}{\partial \tilde{t}} = \tilde{\lambda}^2(\tilde{R}_{\mathrm{ins}} + \tilde{R}_{\mathrm{ext}})\frac{\partial^2\bar{c}}{\partial\tilde{x}^2} + (\tilde{R}_{\mathrm{ins}} - \tilde{R}_{\mathrm{ext}}), \tag{33}$$

where $\tilde{R}_{\mathrm{ins}}$ and $\tilde{R}_{\mathrm{ext}}$ are the dimensionless homogeneous reaction rates

$$\tilde{R}_{\mathrm{ins}} = \left(\frac{1-\bar{c}}{\bar{c}}\right)\mathrm{e}^{\tilde{\mu}_e - \tilde{a}(1-2\bar{c})} \tag{34}$$

$$\tilde{R}_{\mathrm{ext}} = \kappa\left(\frac{\bar{c}^2}{1-\bar{c}}\right)\mathrm{e}^{\tilde{a}(1-2\bar{c}) - \tilde{\mu}_e}. \tag{35}$$

Thus, we see that (32) has a direct analog to a reaction-diffusion equation with a weak, concentration dependent diffusivity and nonlinear source term, in the appropriate physical limit of an atomically sharp phase boundary. The detailed structure and dynamics of the phase boundary, however, must be obtained by solving the full equation (32). Representative plots of the homogeneous net insertion rate $\tilde{R}_{\mathrm{ins}} - \tilde{R}_{\mathrm{ext}}$ are shown in Fig. 3.

3.3. Wave solutions

Eq. (32) admits traveling-wave solutions, which physically correspond to phase-transformation waves, propagating through the crystal with steadily translating depth-averaged concentration profile. In Appendix B, we give technical arguments to show that Eq. (32) has solutions of the form

$$\bar{c}(\tilde{x},\tilde{t}) = g(\tilde{x} - \tilde{v}\tilde{t}), \tag{36}$$

where $g(\zeta)$ is a steady depth-averaged concentration profile in the variable $\zeta = \tilde{x} - \tilde{v}\tilde{t}$. A key conclusion is that the dimensionless velocity $\tilde{v}$ is the same for all fully developed waves. As described below, the eventual shape and velocity of a wave depend only on the physical parameters and not on the initial conditions.

To avoid mathematical complexity, in this section we focus on numerical solutions of (32) to demonstrate how phase-transformation waves are triggered by concentration fluctuations from a globally unfavorable (but locally stable) configuration in the external chemical potential. We solve (32) with an explicit finite

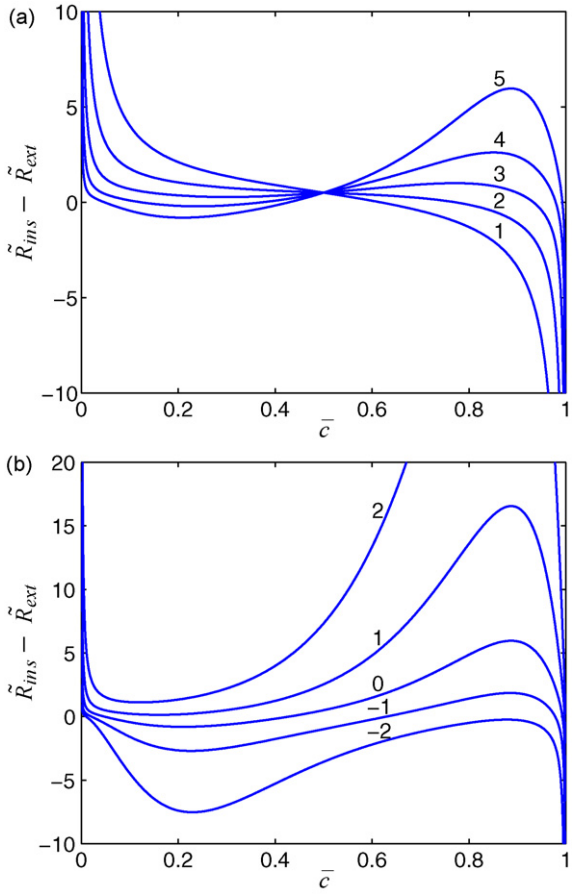

Fig. 3. Dimensionless homogeneous net insertion rate. (a) $\tilde{\mu}_e = 0$, $\kappa = 1$, $\tilde{a} = 1, \ldots, 5$ as labeled in figure. (b) $\tilde{a} = 5$, $\kappa = 1$, $\tilde{\mu}_e = -2, \ldots, 2$ as labeled in figure.

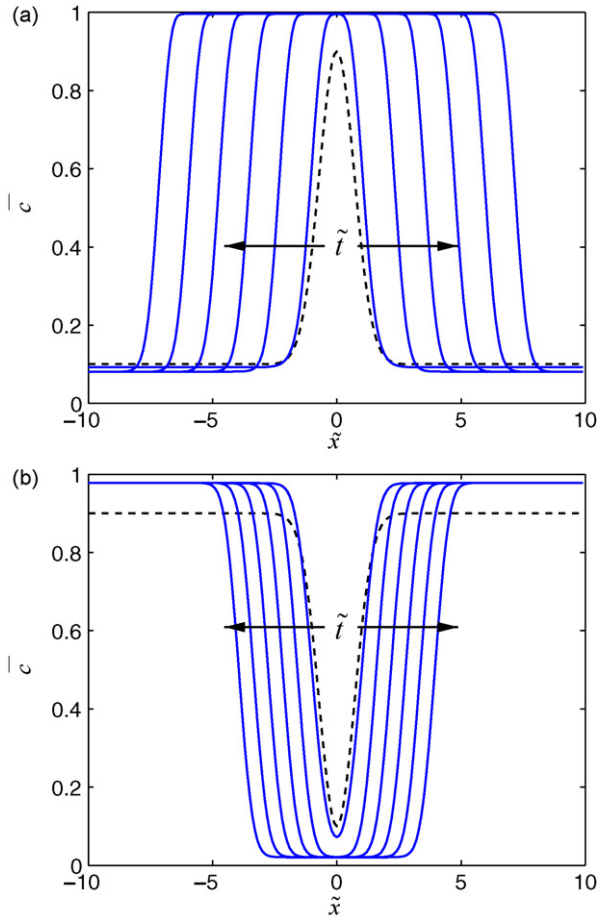

Fig. 4. Numerically computed phase transformation waves during insertion and extraction. Dashed lines show initial conditions; solid lines show concentration profiles at uniformly spaced times, with arrows indicating direction of wave propagation. For both insertion and extraction: $\tilde{a} = 5$, $\kappa = 1$, $\tilde{\lambda} = 1$. (a) Insertion wave with $\tilde{\mu}_e = 0.5$, $\bar{c}(\tilde{x}, 0) = 0.1 + 0.8\exp(-\tilde{x}^2)$. (b) Extraction wave with $\tilde{\mu}_e = -1$, $\bar{c}(\tilde{x}, 0) = 0.9 - 0.8\exp(-\tilde{x}^2)$.

difference method, second order in space and time. Representative phase transformation waves during Li insertion and extraction are shown in Fig. 4. For these simulations, $\tilde{a} = 5$ and $\tilde{\lambda} = 1$, similar to the values given in [19]. The choice of $\tilde{\lambda}$ corresponds to the dimensional lengthscales $\lambda = L = 10$ nm. Although there is no available experimental or simulational data on the rate coefficients k_{ins} and k_{ext}, we expect that the insertion and extraction reactions occur on the same timescale and therefore assume $\kappa = 1$.

Insertion or extraction is forced by raising or lowering the electrolyte chemical potential $\tilde{\mu}_e$ to promote transfer in one direction and inhibit transfer in the other; $\tilde{\mu}_e = 0.5$ for the insertion process in Fig. 4 a, and $\tilde{\mu}_e = -1$ for the extraction process in Fig. 4 b. The initial conditions for the insertion and extraction waves, denoted by dashed lines in the plots, are Gaussian fluctuations of the composition representing nucleations of the lithiated and unlithiated phases, respectively. For the insertion in Fig. 4 a, $\bar{c}(\tilde{x}, 0) = 0.1 + 0.8\exp(-\tilde{x}^2)$, and for the extraction in Fig. 4 b, $\bar{c}(\tilde{x}, 0) = 0.9 - 0.8\exp(-\tilde{x}^2)$.

In the SRL regime, the initial composition fluctuation rapidly develops into two wavefronts bounded by the locally stable equilibrium Li-poor and Li-rich concentrations $\bar{c} = g_1$ and $\bar{c} = g_3$, respectively. This process is driven by the existence of an intermediate, locally unstable equilibrium concentration, $\bar{c} = g_2$, where $0 < g_1 < g_2 < g_3 < 1$. In strongly phase separating systems such as $LiFePO_4$, which correspond to $\tilde{a} \gg 1$ in our model, we have $g_1 \approx 0$, $g_2 \approx 1/2$, and $g_3 \approx 1$. (For definitions of g_1, g_2 and g_3 and approximations for $\tilde{a} \to \infty$, see Appendix B.)

The development of a fully formed wave from a concentration fluctuation involves both insertion and extraction in the vicinity of the wavefront. During the insertion process in Fig. 4 a, the maximum concentration of the initial fluctuation grows to g_3, while the low concentration baseline decays to g_1. Conversely, for the extraction process in Fig. 4 b, the minimum concentration decays to g_1, and the high concentration baseline grows to g_3. Once fully developed wavefronts form, they propagate to the right and left with a constant velocity. We have verified that the velocity of a fully developed wavefront is constant for all times in the numerical simulations, as predicted by the analysis in Appendix B.

Not all initial conditions give rise to traveling waves, as shown in Fig. 5. The key requirement for the formation of traveling waves is that the initial condition supports both addition and removal of Li in the domain, that is $R(x, 0)$ must change sign. The simultaneous addition and removal of material sharpen the initial composition fluctuation to a phase separating wavefront. In the failed insertion event shown in Fig. 5 a, only extraction occurs, and the initial composition perturbation decays to a uniform concentration of g_1. Similarly, Fig. 5 b presents a failed extraction event where the initial composition depression fills up to a uniform concentration of g_3. Note that $R(x, 0)$ depends on the Laplacian of the initial concentration profile $\bar{c}(x, 0)$, and thus different initial conditions with equal composition ranges but varying spatial distributions will or will not produce traveling waves. This behavior has been numerically verified.

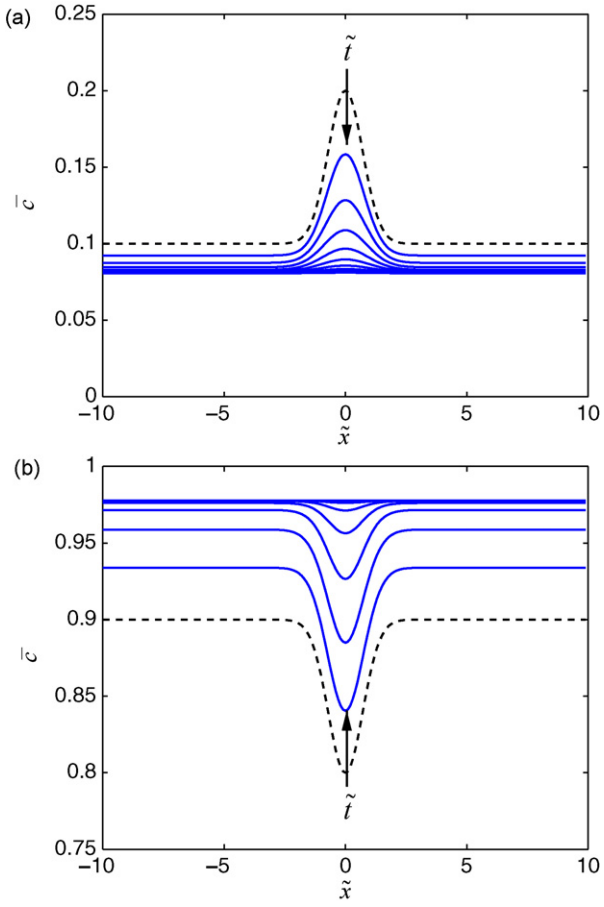

Fig. 5. Numerically computed failed insertion and extraction events. Dashed lines show initial conditions; solid lines show concentration profiles at uniformly spaced times, with arrows indicating direction of profile movement. For both insertion and extraction: $\tilde{a} = 5$, $\kappa = 1$, $\tilde{\lambda} = 1$. (a) Failed insertion event with $\tilde{\mu}_e = 0.5$, $\bar{c}(\tilde{x}, 0) = 0.1 + 0.1\ \exp(-\tilde{x}^2)$. (b) Failed extraction event with $\tilde{\mu}_e = -1$, $\bar{c}(\tilde{x}, 0) = 0.9 - 0.1\ \exp(-\tilde{x}^2)$.

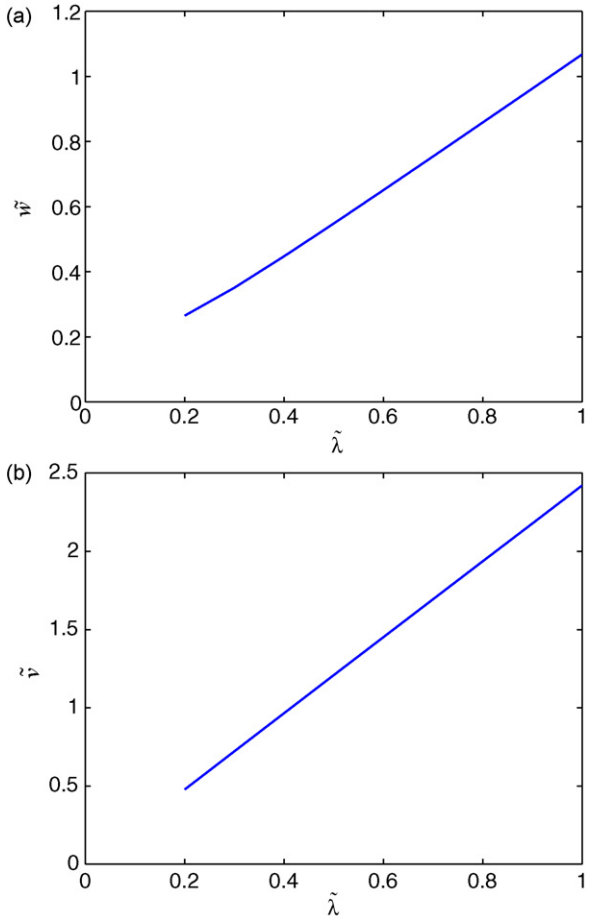

Fig. 6. Scaling of computed wave (a) width and (b) velocity with $\tilde{\lambda}$. Parameters: $\tilde{a} = 5$, $\kappa = 1$, $\tilde{\mu}_e = 0.5$, $\bar{c}(\tilde{x}, 0) = 0.1 + 0.8\ \exp(-\tilde{x}^2)$.

The dependence of the formation of traveling waves on the initial condition relates to the nucleation of the phase separation. When a fluctuation is too small so that its amplitude does not reach the spinodal limits or its spatial extent is too small, it will decay, but heterogeneous nucleation may change this behavior. During insertion, for example, the lithiated phase may first nucleate at some atomic scale inhomogeneity on the crystal surface where it is energetically favorable for Li atoms to collect. Our theory does not account for such features. Moreover, as the $FePO_4$/$LiFePO_4$ phase boundary width λ is nearly at the atomic scale, applying a continuum equation for nucleation below this scale may not be physically relevant. We note, however, that continuum nucleation could be studied in other SRL systems with larger λ.

3.4. Scalings of the wave width and velocity

The crucial properties of an SRL wave are its velocity and width, each of which depend on physical parameters in ways that could be experimentally accessible. The wave velocity is related to the current versus time in response to an applied voltage, or vice versa, as explained in the next section. The wave width could in principle be observed by removing the driving force for the phase transformation and measuring the concentration profile.

The dependence of any quantity of interest on the physical parameters can be obtained by dimensional analysis [32], supplemented by numerical simulations to calculate dimensionless scaling functions. For example, considering the units of the physical parameters, the wave width can be written in the general form,

$$w = LF_w\left(\frac{\lambda}{L}, \frac{a}{\rho kT}, \frac{\mu_e}{\rho kT}, \frac{k_{ext}}{k_{ins}}\right) \tag{37}$$

where $F_w(\tilde{\lambda}, \tilde{a}, \tilde{\mu}_e, \kappa)$ is a scaling function. Since the width w should not depend on the size of the crystal L in the limit of a sharp phase boundary, we must have $\tilde{w} = F_w \sim \tilde{\lambda} f_w$ or $w \propto \lambda$ for $\tilde{\lambda} \ll 1$, consistent with the numerical solutions above in Fig. 6 a. With units restored, this simple argument shows that the width is set by the bulk phase-boundary thickness

$$w \sim \lambda f_w\left(\frac{a}{\rho kT}, \frac{\mu_e}{\rho kT}, \frac{k_{ext}}{k_{ins}}\right), \quad \text{where } \lambda = \sqrt{\frac{K_x}{\rho kT}} \tag{38}$$

as expected, although it may also depend weakly on $\tilde{a}$, $\tilde{\mu}_e$, and κ. A slice of the $\tilde{\mu}_e$ dependence is shown in Fig. 7 a.

From dimensional analysis, the wave speed has a similar form,

$$v = \frac{L}{\tau}F_v\left(\frac{\lambda}{L}, \frac{a}{\rho kT}, \frac{\mu_e}{\rho kT}, \frac{k_{ext}}{k_{ins}}\right) \tag{39}$$

where $F_v(\tilde{\lambda}, \tilde{a}, \tilde{\mu}_e, \kappa)$ is another scaling function. Once again, the limit of a sharp phase boundary requires, $\tilde{v} = F_v \sim \tilde{\lambda} f_v$ or $v \propto \lambda/\tau$ for $\tilde{\lambda} \ll 1$, consistent with the numerical solutions in Fig. 6 b.

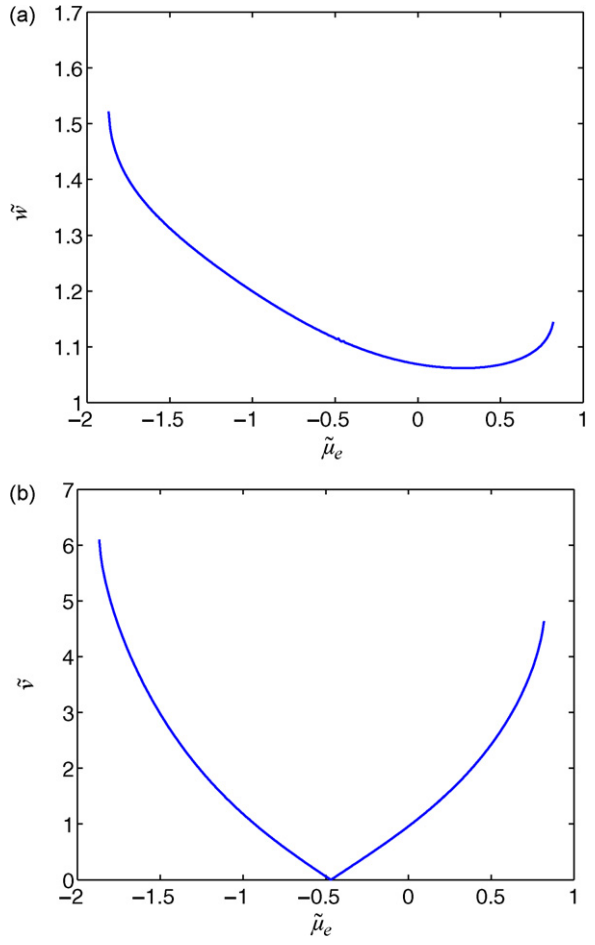

Fig. 7. Dependence of computed wave (a) width and (b) velocity on $\tilde{\mu}_e$. Parameters: $\tilde{a} = 5, \kappa = 1, \tilde{\lambda} = 1, \tilde{c}(\tilde{x}, 0) = g_1(\tilde{\mu}_e) + (1/2)(g_3(\tilde{\mu}_e) - g_1(\tilde{\mu}_e))(\tanh(\tilde{x}) + 1)$.

Recalling the time unit, we obtain a general expression for the wave speed in the limit of a sharp phase boundary,

$$v \sim \frac{\lambda}{\tau} f_v\left(\frac{a}{\rho kT}, \frac{\mu_e}{\rho kT}, \frac{k_{ext}}{k_{ins}}\right), \quad \text{where } \lambda \cdot \tau^{-1} = \sqrt{\frac{K_x}{\rho kT}} \cdot \frac{2\rho_s k_{ins}}{\rho L_y}. \tag{40}$$

Note that the wave speed decreases with increasing crystal thickness, $v \propto (1/L_y)$ since it takes longer for reactions to fill each bulk channel, as the SRL phase transformation sweeps across the crystal. The speed is also proportional to the bulk concentration-gradient penalty K_x and the insertion rate constant k_{ins}. It also should decrease with the strength of the interaction between ions in the crystal a, which drives phase separation. The wave velocity can also be controlled externally by varying the chemical potential of ions in the electrolyte μ_e, as shown in Fig. 7 b.

The velocity formula (40) has a clear physical interpretation in terms of the surface-reaction-limited current. In the limit of a sharp phase boundary, the velocity $v \approx \lambda/\tau$ is the product of the typical reaction rate τ^{-1} for filling or emptying ion channels by surface reactions and the wave width $w \approx \lambda$. The reaction rate τ^{-1} sets the magnitude of the current density at the surface, while the width λ sets the scale for the (propagating) region over which the current density is localized. This interpretation is consistent with the physical picture of the SRL dynamics in Fig. 2.

3.5. Numerical study of wave properties

The scalings above can be verified by numerical simulations, which also map out the dimensionless scaling functions for $\tilde{w}$ and $\tilde{v}$ as the dimensionless parameters are varied. The main parameter controlling the wave width is $\tilde{\lambda}$, since it contains the gradient energy coefficient K_x. As $\tilde{\lambda}$ is decreased, the energetic penalty for forming gradients in the concentration is lowered, resulting in sharper wavefronts spanning the equilibrium phase compositions. Additionally, we find that sharper wavefronts move at a slower velocity. The numerically computed dependence of the width and velocity on $\tilde{\lambda}$ is shown in Fig. 6. It is apparent that both $\tilde{w}$ and $\tilde{v}$ scale linearly with $\tilde{\lambda}$ in the range of physical relevance, as predicted above for the sharp interface limit $\tilde{\lambda} \ll 1$.

The electrolyte chemical potential $\tilde{\mu}_e$ is an experimentally accessible independent parameter, as it corresponds to the applied potential of the system, forcing Li insertion or extraction to occur. Thus, it is important to consider the dependence of the wave width and velocity on this parameter, as a systematic study of this dependence may eventually lead to an experimentally feasible method of testing the SRL model. Fig. 7 shows the numerically determined dependence of $\tilde{w}$ and $\tilde{v}$ on $\tilde{\mu}_e$. As shown in Fig. 7 a, the wave width exhibits a weak, nonlinear dependence on $\tilde{\mu}_e$, embodied in the scaling function F_w defined above.

The velocity dependence in Fig. 7 b shows how the system transitions from extraction waves to insertion waves as $\tilde{\mu}_e$ increases from negative to positive. Large negative values of $\tilde{\mu}_e$ strongly force Li removal, resulting in extraction waves with large velocities. As $\tilde{\mu}_e$ increases, the extraction wave velocity declines steeply, until zero velocity is obtained at $\tilde{\mu}_e \approx -0.5$. This point is the transition from extraction to insertion. Insertion waves with increasing velocities are produced as $\tilde{\mu}_e$ increases beyond the transition point. Analogously to the width, the velocity dependence is contained within a scaling function, F_v defined above.

Note that the width and velocity profiles in Fig. 7 are not symmetric about the transition point, and the minimum width does not correspond to zero velocity. The asymmetry in the width and velocity result from the asymmetry in the homogeneous net reaction rate. As noted above, $\tilde{R}_{ins} - \tilde{R}_{ext}$ must have three roots g_1, g_2 and g_3 over the composition range $0 < c < 1$ in order for phase separation to occur. This requirement imposes a restricted range $\tilde{\mu}_e^- < \tilde{\mu}_e < \tilde{\mu}_e^+$ for SRL dynamics to be observed for a given set of parameters.

The critical values $\tilde{\mu}_e^{\pm}$ are derived in Appendix B, and here we explain the physical reason for such limits to exist for SRL waves. Of course, phase transformation dynamics can be driven by an arbitrarily positive or negative $\tilde{\mu}_e$, but there are transitions between the different fundamental modes illustrated in Fig. 2 and defined in Eqs. (21)–(25). A large electrochemical potential, $\tilde{\mu}_e < \tilde{\mu}_e^-$ or $\tilde{\mu}_e > \tilde{\mu}_e^+$, effectively increases the overall surface reaction rate k and pushes the system out of the SRL regime ($Da_y \ll 1$) by making bulk transport in the Li channels rate limiting. Indeed, for sufficiently fast surface reactions, the system becomes a BTL process ($Da_y \gg 1$) with phase transformation governed by shrinking-core-type dynamics. We leave a detailed analysis of this dynamical transition in our general model for future work. This would be worthwile since experiments may be able to probe the transition by varying the chemical potential or other parameters and observing changes in current–voltage characteristics or concentration profiles.

4. Current in response to an applied voltage

4.1. BTL versus SRL dynamics

Transport in electrode materials is often studied by measuring the current response of the material to an applied potential.

In an isotropic BTL process, a potential step induces a current proportional to the diffusion limited flux of ions across the electrode/electrolyte interface. The response time of any linear or nonlinear diffusion limited process, such as assumed in the shrinking core model, is given by the characteristic time t_D. The flux for small times, and hence the current, can be found analytically from the similarity solution for diffusion in a semi-infinite domain. The resulting expression for the current is known as the Cottrell equation,

$$I_{\text{Cottrell}} = neA\rho\sqrt{\frac{D}{\pi t}}, \quad t \ll t_D, \tag{41}$$

where n is the number of electrons transferred and A is the electrode particle area. The Cottrell current response forms the basis of the Potentiostatic Intermittent Titration Technique (PITT) that is commonly used to measure the diffusivity of materials [33]. However, cathodes that operate in a SRL transport regime where bulk diffusion in a preferred direction is fast relative to ion transfer at the electrode/electrolyte interface cannot be assumed to follow Cottrell dynamics.

In our model for single crystal $LiFePO_4$, the chemical potential of the electrolyte μ_e serves as the applied potential to the system. For an appropriate μ_e, sharply defined waves of Li propagate across the crystal surface as Li transfer occurs. A composition fluctuation initiates each wave, and all fully developed waves in the system travel with the same, constant velocity, in a flat plate-like particle. The total flux of ions across the two xz surfaces of the crystal is determined by the integral of the net insertion rate, so the current response of a single crystal is given by

$$I = ne\iint \rho_s R\,dx\,dz, \tag{42}$$

Note that since the reaction rate R is zero at the equilibrium phase compositions g_1 and g_3, only localized wavefronts spanning these compositions contribute to the current.

The scaling of the SRL response is completely different from that of the Cottrell BTL response. Ignoring geometrical effects and nucleation (discussed below), the response time for a single crystal is given by the time L_x/v for a wave to cross it, which has the following scaling for thin interfaces:

$$t_v = \frac{L_x\tau}{\lambda} = L_x\sqrt{\frac{\rho kT}{K_x}}\frac{\rho L_y}{2\rho_s k_{\text{ins}}}. \tag{43}$$

Note that the response time is proportional to two geometrical lengths, the depth of the channels L_y and the length L_x over which the waves are propagating. More importantly, the time is determined by the surface reaction rate k_{ins} and not by the bulk diffusion coefficient D_x. The ratio of the time scales for BTL dynamics and SRL dynamics is an effective Péclet number,

$$Pe_x = \frac{t_x^D}{t_v} = \frac{vL_x}{D_x} = \sqrt{\frac{K_x}{\rho kT}}\frac{2\rho_s k_{\text{ins}}L_x}{\rho L_y D} \tag{44}$$

which measures the importance of wave propagation at the diffusive time scale. However, this is once again the Damkohler number, since the reaction time is set by wave propagation, $t_x^R = t_v$, in the SRL regime.

4.2. Plate-like crystals

To develop a general picture of SRL phase transformation dynamics in a rechargeable-battery intercalation material, we first consider the case of flat plate-like crystals of constant depth L_y analyzed in the previous section. A fully developed wavefront moving with constant velocity supports a steady current, and there is a sudden loss in the current when two wavefronts merge and are replaced by an equilibrium composition. Fig. 8 shows this declining staircase form for the current in a system with two impinging waves. The spike in the current at the time of collision is due to the gradient penalty term in the reaction rate acting on the sharp composition profile of the merging waves. We note that the magnitude of the spike is large in this simulation since there are only two waves; in an actual system with many waves, the surge in current from any individual collision would be small relative to the total current being sustained.

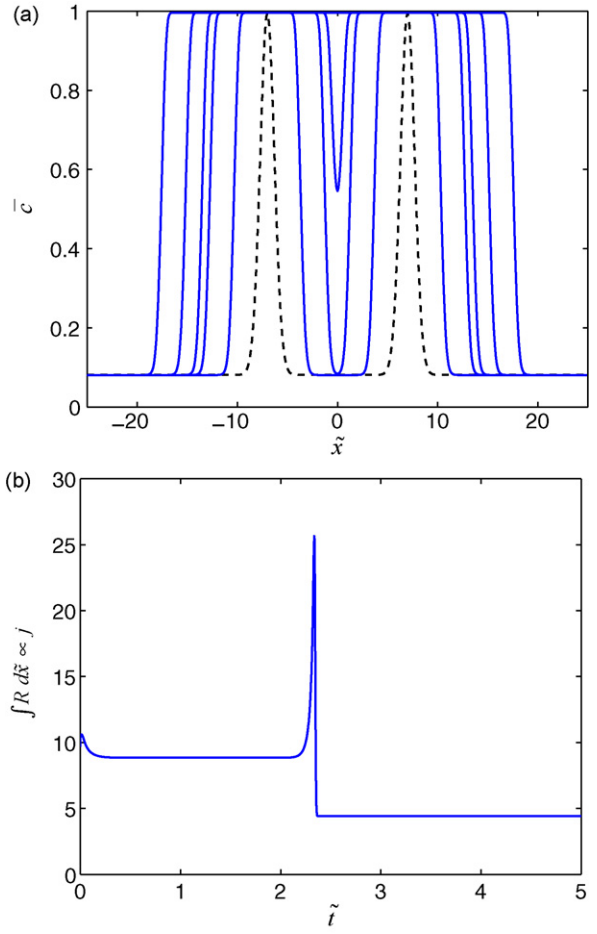

Fig. 8. Numerically computed phase transformation dynamics and flux response of two impinging insertion waves. (a) Concentration profiles of impinging waves. Dashed line shows initial condition; solid lines show concentration profile at various times during impingement. (b) Flux response of impinging waves. Parameters: $\tilde{a} = 5$, $\kappa = 1$, $\tilde{\lambda} = 1$, $\tilde{\mu}_e = 0.5$, $\tilde{c}(\tilde{x}, 0) = g_1 + (g_3 - g_1)[\exp(-(\tilde{x}+7)^2) + \exp(-(\tilde{x}-7)^2)]$.

Therefore, the current response of $LiFePO_4$ is governed by the overall rate of its transformation through concurrent nucleation and growth of waves. Phase nucleation likely occurs by both heterogeneous and homogeneous mechanisms. Recent first principles computations have found that the chemical potential of Li varies considerably over the surface of the equilibrium crystal shape [29]. Consequently, different crystal faces may be energetically favorable for heterogeneous phase nucleation during Li insertion and extraction.

An example of a single crystal undergoing heterogeneous and homogeneous nucleation and growth is illustrated in Fig. 9. Fig. 9 a shows xy cross sections of the crystal at a sequence of successive times $t_1, \ldots, t_6$, and Fig. 9 b presents the corresponding profile of the total current I. At time t_1, heterogeneous nucleation at the crystal edges has produced two fully developed wavefronts, each

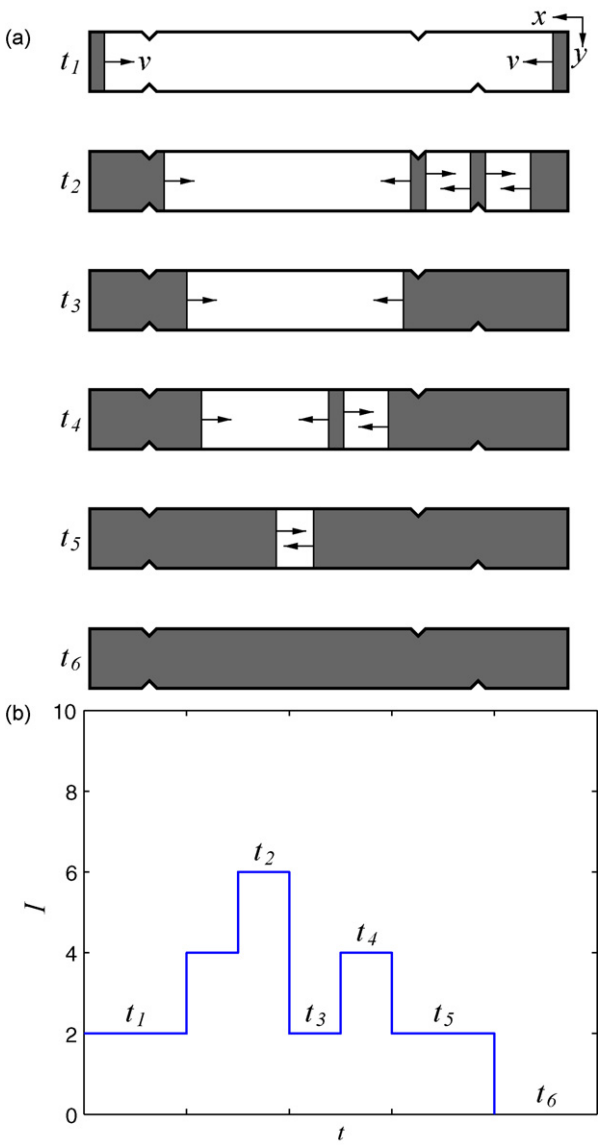

Fig. 9. Schematic diagram of overall phase transformation and current response of a single plate-like crystal undergoing SRL transport. (a) Sequence of *xy* cross sections of crystal at times $t_1, \ldots, t_6$, illustrating phase transformation of material through concurrent nucleation and growth of traveling waves. Each fully developed wavefront moves with velocity v and sustains a constant current of unity. (b) Declining staircase current response of crystal, with labeled times corresponding to illustrations in (a).

moving with constant velocity v and sustaining a normalized current of unity. Therefore, the crystal supports the total current $I = 2$ at this time. At some time between t_1 and t_2, heterogeneous nucleation occurs at the two rightmost surface defects of the crystal, indicated by notches. Once these nucleation events grow into fully developed waves, there are six propagating wavefronts carrying a total current of $I = 6$. The rightmost waves merge at time t_3 such that four wavefronts are destroyed, and consequently, only two traveling wavefronts remain and the current drops to $I = 2$. Homogeneous nucleation at some location in the untransformed fraction of the material occurs at time t_4, and the two additional wavefronts created increase the current to $I = 4$. The rightmost waves combine at time t_5, and as most of the material is transformed and only two wavefronts remain, the current again drops to $I = 2$. Finally, at time t_6, the material is fully transformed and can no longer sustain a current.

4.3. Other crystal shapes

The wave dynamics can depend sensitively on the crystal *shape* in the SRL regime. This general fact can be easily seen from our analysis of a plate-like crystal: the wave velocity (40) depends on the local depth $L_y(x, z)$ of the fast diffusion channels in the bulk, as well as the local surface orientation, through the surface-site density $\rho_s(x, z)$. The analysis of SRL phase-transformation dynamics for arbitrary crystal shapes is a challenging problem, left for future work.

Here, we simply indicate how scalings by considering the limit of slowly varying depth, $L_y(x)$, and assuming the 1D wave dynamics for a flat surface are only slightly perturbed. The local wave velocity is then

$$v = \frac{\mathrm{d}x_w}{\mathrm{d}t} = \frac{D_w}{L_y(x_w)} \tag{45}$$

where $D_w = 2\rho_s(x_w)k_{\mathrm{ins}}\sqrt{K_x/(\rho^3 kT)} \approx$ constant. This ordinary differential equation can be solved for the position of the wave $x_w(t)$ from a given wave nucleation event for any slowly varying shape $L_y(x_w)$. For example, consider the case of a cylinder, $L_y(x) = \sqrt{R^2 - x^2}$ (ignoring that the shape is not slowly varying at the ends). In that case, the equation can be solved analytically, e.g., for nucleation at one edge $x = -R$. For early times, the wave velocity decays from its initial value as $\mathrm{d}x_w/\mathrm{d}t \propto D_w^{2/3} t^{-1/3}$, due to the increasing depth of the bulk channels.

In spite of variable wave speed, however, the current remains constant during wave propagation in this approximation, as in the case of a flat plate, regardless of the crystal shape. The reason is that wave propagation at speed $v(x_w)$ engulfs channels of length $L_y(x_w)$, so the total current, proportional to vL_y, remains constant according to (45). The time for a wave to engulf the entire crystal thus scales with the total volume (in contrast to diffusive BTL dynamics, where the time scales like the cross-sectional area). Physically, ions are being inserted or extracted at roughly a constant rate, since the phase boundary is assumed to have a constant exposed length at the surface for 1D dynamics.

For spheres and other 3D shapes, the wavefront will not remain flat, and the full 2D depth-integrated dynamics will need to be solved with variable $L_y(x, z)$ and $\rho_s(x, z)$. However, the current may remains roughly constant during wave propagation, since the filling time for a channel is proportional to its length, at constant surface reaction rate. In that case, the results of the previous section for current versus time in flat plate-like single crystals may not be substantially modified with more complicated shapes, although statistical fluctuations due to random nucleation events will be different.

4.4. Composite cathode response

It is important to note that Fig. 9 represents only one possible realization of the transformation and current response of the crystal. Heterogeneous nucleation may occur at different edges or surface defects at different times for different insertion and extraction cycles. Homogeneous nucleation would be spatially distributed in some random fashion. Therefore, to determine the overall current response of a composite cathode composed of many individual crystals, we must consider the statistical distributions of the nucleation events.

For homogeneous nucleation, we may assume that the nucleation rate is uniform across the crystal surface. Nucleation events in the untransformed material are independent, and the presence of a previously nucleated wave does not influence the likelihood of nucleation around that wave. With these assumptions, the nucle-

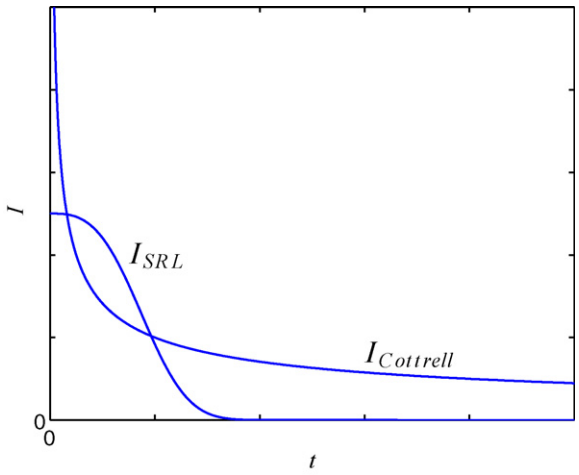

Fig. 10. Schematic illustration of composite cathode responses for Cottrell (BTL) and SRL phase transformation mechanisms.

ation events are distributed as a Poisson process in time, and we may invoke the Johnson–Mehl–Avrami equation for the overall transformation rate of the material [34]

$$\xi = e^{-Gt^m}, \tag{46}$$

where ξ is the untransformed fraction of the material, G a factor dependent on the dimensionality of the process, and the integer $m > 1$; for a 1D line nucleation process, $Gt^m \sim t^2$. The Johnson–Mehl–Avrami equation therefore specifies that the overall transformation rate of the material follows a sigmoidal shape. We thus expect that the current also follows this sigmoidal response for concurrent homogeneous nucleation and growth.

In the case of heterogeneous nucleation, we may assume that for many defects in many particles, the heterogeneous nucleation events are distributed as a Poisson process in space. Thus, the qualitative form of the average response is expected to follow the same sigmoidal shape as homogeneous nucleation, assuming all electrode particles are at the same potential (driving force), which may only be true under low rate conditions or for thin electrodes [4,35].

Thus, we have found that individual crystals have a declining staircase form for their current response to an applied electrolyte potential μ_e if a substantial number of nucleation events occur on the timescale of complete transformation. For many crystals, we may consider that the homogeneous and heterogeneous nucleation events are Poisson processes in time and space, respectively. The overall transformation and current response of the material is then given by the average of many distinct staircase responses, resulting in a characteristic sigmoidal curve

$$I \propto e^{-Gt^m}, \tag{47}$$

which is strikingly different from the Cottrell response that is commonly assumed. Fig. 10 compares the sigmoidal and Cottrell responses. We conclude that PITT measurements in material undergoing SRL transport do not measure the diffusivity. Rather, these measurements provide some measure of the kinetic parameters in the surface reaction rates that are controlling the overall rate of the material transformation.

4.5. Discussion

The model we propose is based on a few key experimental and theoretical findings. (i) Li migrates rapidly in the (0 1 0) direction (y in Fig. 1) creating either filled or empty channels that completely penetrate the material. This makes it possible to coarse-grain to a two-dimensional model in which the surface concentration defines the concentration in a channel. (ii) A linear interface exists on the particle surface between filled and unfilled sites, and growth of one phase at the expense of the other occurs by displacement of this interface. Such one-dimensional growth is supported by experimental observations [15] and by a recent Johnson–Mehl–Avrami analysis of the growth exponents [36]. Since one would expect two-dimensional growth on the surface for an isotropic material, the one-dimensional growth has to find its origin in the crystallography of the material. Undoubtedly, it is either the anisotropy of the interfacial strain energy—due to different coherence strains or elastic constants [11], or the anisotropy of the interfacial energy which causes the system to prefer a single interface plane. The most likely interface plane has been deduced from TEM observations of cracks on electrochemically cycled particles indicating that for platelet shaped particles with large (0 1 0) surface area, the (1 0 0) interface orientation is preferred.

In our model the Li current distribution on the (0 1 0) surface is localized at the $LiFePO_4/FePO_4$ interface region because the fully (de)lithiated regions provide either no Li(vacant sites) or cannot nucleate the other phase upon charge(discharge). The interfacial width and the free energy of the Li ions at the interface thus play key roles in the current rate that can be sustained. As the interface becomes wider, more sites on the surface can participate in the transfer reaction to(from) the electrolyte and the interface velocity increases, as can be observed in Fig. 6. As long as this interface remains unchanged as it moves across the particle surface, the transformation rate is nominally constant, until the particle is either fully transformed, new nucleation events occur, or two wave fronts impinge. This is fundamentally different from the core–shell model in which the ability of the particle to take up current declines as the transformation proceeds. Note that such transformation kinetics is also fundamentally different from Cottrell-like behavior, which may demand reinvestigation of how one extracts atomistic level parameters from rate measurements.

How this new phase-transformation kinetics manifests itself in the observable voltage-current response may depend very much on the structure of the macroscopic electrode in which the active $LiFePO_4$ particles are embedded. In addition to the active material, a typical electrode contains about 5–10 wt% polymeric binder and 5–15 wt% carbon black to enhance electronic conductivity through the electrode. Some porosity is also created in the electrode to allow the electrolyte to penetrate and transport the Li^+ ions to and from the active material. If the conductive pathways for the Li^+ ions and electrons are sufficient, all particles will be at the same potential and experience a similar driving force for transformation. Under these conditions, and assuming stochastic nucleation, we expect that the overall current response to a potential pulse is sigmoidal. Recent work indicates that such equipotential conditions across the electrode only apply at rather low charge and discharge rates, or for very thin electrodes [35]. If such electrical resistance along the thickness of the electrode plays a role, the collective current response of the system could be viewed as of a sum of sigmoidals, each with a different driving force, but time-dependent screening effects would also need to be taken into account.

5. Conclusion

We have proposed a general continuum theory for phase-transformation dynamics in single-crystal intercalation compounds, such as those used in rechargeable battery electrodes. The bulk transport model is based on a thermodynamically sound phase-field formulation of the free energy. Unlike standard approaches to electrochemical kinetics, the chemical potential from

the phase-field model, including the gradient energy penalty, also influences surface reaction rates. The general theory may be useful in modeling a range of battery electrode materials, including intercalation compounds that form solid solutions, with rate-limiting slow diffusion.

In cases of strong phase separation, the general theory describes several types of dynamics for a sharp phase boundary, depending on the characteristic timescales for bulk transport and surface reactions (or Damkohler numbers) in different crystal directions. For example, in cases of fast reactions, the theory captures the existing spherical shrinking-core picture, as well as more general bulk-transport-limited models. In the limit where fast diffusion in one direction equilibrates the bulk concentration to the surface concentration, the same general model reduces to a new type of equation describing anisotropic surface-reaction-limited phase-transformation dynamics. We find that this reduced model exhibits traveling-wave solutions, which qualitatively agree with the experimental observations of the phase boundary in $LiFePO_4/FePO_4$. The SRL model may also have relevance for other materials (not only in battery electrodes) where surface transfer effects are rate limiting, such as nanoporous materials.

Our model has fundamental implications for the interpretation of experimental data for rechargeable batteries. For example, the Cottrell equation of isotropic BTL dynamics is commonly used to infer the bulk diffusivity from the current response to an applied voltage, and this is indeed one simple limit of our general model. However, using the same model, we show that in the SRL regime, such a measurement could infer only the surface reaction rate, and not the bulk diffusivity. These new concepts may be crucial for experimental studies of $LiFePO_4$in particular, since recent observations of the phase boundary in this material are consistent with SRL waves and not BTL shrinking-core dynamics.

Our work also focuses attention to the importance of the Li^+ and electron delivery to the proper surface of $LiFePO_4$ in order to achieve fast charge absorption. While much effort in the experimental literature has focused on electron delivery (e.g. by carbon coating or conductive Fe_2P contributions) [37,38], little emphasis seems to have been placed on rapid transport of Li^+towards the surface where it can penetrate. The model presented here may thus serve as a simple starting point to guide the development of improved electrode materials.

Acknowledgments

This work was supported by the MRSEC program of the National Science Foundation under award number DMR 02-12383. The authors thank K. Thornton and D. Burch for helpful comments on the manuscript.

Appendix A. Nomenclature

a	average energy density of ion interaction [E/ L^3]
$\tilde{a}$	dimensionless interaction coefficient a
A	host material surface area [L^2]
$\mathbf{B}$	mobility tensor [L^2/(ET)]
c	dimensionless, normalized ion concentration
$\bar{c}$	depth-averaged Li concentration
c_e	ion concentration in the electrolyte
c_{sp}	spinodal compositions
$c_\pm$	equilibrium phase compositions of homogeneous free energy $\bar{f}$
$\mathbf{D}$	diffusivity tensor [L^2/T]
D_w	constant entering the wave position [L^2/T]
D_i^{eff}	effective Fickian diffusivities [L^2/T]
$\mathbf{D}^{chem}$	chemical diffusivity tensor [L^2/T]
Da_x, Da_y, Da_z	Damkohler numbers $= t_i^D/t_i^R$
f_v	reduced scaling function for wave velocity
f_w	reduced scaling function for wave width
$\bar{f}$	homogeneous free energy density [E/ L^3]
F	total free energy of the intercalation crystal [E]
F_v	scaling function for wave velocity
F_w	scaling function for wave width
g	Li concentration in traveling wave solution
g_1, g_3	equilibrium phase compositions of traveling wave solution
g_2	unstable intermediate composition of traveling wave solution
$g_\pm$	composition extrema of (52)
G	dimensionality factor in Johnson–Mehl–Avrami equation [1/T^m]
h	derivative of g in traveling wave solution
I	current response [C/T]
$I_{Cottrell}$	Cottrell current [C/T]
$\mathbf{j}$	bulk ion flux [1/(L^2T)]
$\mathbf{j}_s$	surface ion flux density [1/(LT)]
k	Boltzmann's constant [E/ T_K]
k_{ext}	extraction rate coefficient [1/T]
k_{ins}	insertion rate coefficient [1/T]
$\mathbf{K}$	phase-field gradient-penalty tensor [E/L]
L_i	characteristic lengthscales of the crystal [L]
L_y	y direction depth profile [L]
m	integer exponent in Johnson–Mehl–Avrami equation
n	number of electrons transferred across electrode/electrolyte interface
$\mathbf{n}$	unit normal vector out of crystal
Pe	Péclet number
R	net ion insertion rate [1/T]
R_{ext}	ion extraction rate [1/T]
$\bar{R}_{ext}$	homogeneous ion extraction rate [1/T]
$\tilde{R}_{ext}$	dimensionless homogeneous Li extraction rate
R_i	characteristic reaction rates [1/T]
R_{ins}	ion insertion rate [1/T]
$\bar{R}_{ins}$	homogeneous ion insertion rate [1/T]
$\tilde{R}_{ins}$	dimensionless homogeneous Li insertion rate
$\tilde{t}$	dimensionless time
t_v	characteristic time for SRL phase transformation [T]
t_i^D	timescales for bulk diffusion ($i = x, y, z$) [T]
t_i^R	timescales for surface reactions [T]
T	absolute temperature [T_K]
v	dimensional velocity of traveling wave [L/T]
$\tilde{v}$	dimensionless constant velocity of traveling wave solution
w	dimensional width of traveling wave [L]
$\tilde{w}$	dimensionless width of traveling wave
x	ion filling fraction
x, y, z	crystal directions defined in Fig. 1
$\tilde{x}$	dimensionless length
x_w	wave position [L]

Greek letters

β	$1/(\rho kT)$ [L^3/E]
Γ	dimensionless parameter introduced in (52)
δ_{ij}	Kronecker delta function
ϵ	equilibrium composition in the shrinking-core model
ζ	reduced coordinate of traveling wave solution
κ	dimensionless rate coefficient
λ	characteristic lengthscale of phase boundary [L]

$\tilde{\lambda}$	dimensionless gradient energy coefficient
μ	chemical potential of ions in the host crystal [E/ L^3]
$\tilde{\mu}$	homogeneous chemical potential [E/ L^3]
μ_e	chemical potential of ions in the electrolyte [E/ L^3]
$\tilde{\mu}_e$	dimensionless chemical potential of Li in the electrolyte
$\tilde{\mu}_e^{\mp}$	bounding values of $\tilde{\mu}_e$ for traveling wave solutions
∇_s	surface gradient [1/L]
ξ	untransformed fraction of material
ρ	number of intercalation sites per unit volume [$1/L^3$]
ρ_s	surface intercalation sites per unit area [$1/L^2$]
τ	characteristic timescale for SRL waves [T]

Appendix B. Existence of SRL waves

In this section, we provide some mathematical details regarding the dynamics of the depth-averaged concentration $\bar{c}$ in the SRL regime of our general phase-transformation model. In particular, we study the existence of traveling-wave solutions to Eq. (32) of the form

$$\bar{c}(\tilde{x},\tilde{t}) = g(\tilde{x}-\tilde{v}\tilde{t}), \tag{48}$$

where $g(\zeta)$ is a steady depth-averaged concentration profile in the variable $\zeta = \tilde{x}-\tilde{v}\tilde{t}$ propagating at a constant dimensionless velocity $\tilde{v}$. Substituting Eq. (48) into Eq. (32), the partial differential equation is reduced to a second-order, nonlinear ordinary differential equation for $g(\zeta)$.

In order to investigate its possible solutions, it is convenient to rewrite it as a system of two nonlinear first-order equations,

$$\frac{dg}{d\zeta} = h, \tag{49}$$

$$\frac{dh}{d\zeta} = \frac{1}{\tilde{\lambda}^2}\ln\left[\frac{-\tilde{v}h+\sqrt{(\tilde{v}h)^2+4\kappa g}}{2\tilde{R}_{ins}(g)}\right], \tag{50}$$

which defines a vector "velocity field" $\left(dg/d\zeta, dh/d\zeta\right)$ for solution trajectories in the (g,h) "phase plane" (not to be confused with chemical phases described in the main text), where ζ acts as "time". From this standard mathematical perspective, the qualitative behavior of solutions is controlled by critical points of the vector field in the phase plane. In this case, there are stationary points given by

$$h = 0, \tag{51}$$

$$\tilde{a}(1-2g)+\ln\left(\frac{g^{3/2}}{1-g}\right)+\ln\Gamma = 0, \tag{52}$$

where we have defined another dimensionless constant $\Gamma = e^{-\tilde{\mu}_e}\sqrt{\kappa}$. By studying solutions to this algebraic equation, we can establish general features of solutions of the original problem without actually solving for $g(\zeta)$.

The solutions of (52) correspond to the roots of the spatially homogeneous source $\tilde{R}_{ins}-\tilde{R}_{ext}$ and therefore determine the equilibrium phase compositions of the system. Explicit expressions for the solutions are not possible, though at least one solution must exist, since the left hand side changes sign over the interval $0<g<1$. However, phase separation into Li-poor and Li-rich phases requires three solutions $g_1<g_2<g_3$, where g_1 and g_3 are the equilibrium compositions bounding the moving wavefront, and g_2 is an unstable intermediate composition. We observe that the phase compositions are independent of the dimensionless gradient penalty $\tilde{\lambda}^2$. At the threshold where (52) transitions from one solution to three, the solutions and extrema of the equation coincide. The extrema occur at the compositions

$$g_{\pm} = \frac{(1+4\tilde{a})\pm\sqrt{16\tilde{a}^2-40\tilde{a}+1}}{8\tilde{a}}, \tag{53}$$

and as two distinct extrema are needed for three solutions of (52), phase separation requires $\tilde{a}>(5/4)+\sqrt{3/2}\approx 2.47$. If the minimum $\tilde{a}$ is exceeded, (52) can be used to compute the rate coefficients and electrolyte chemical potential, expressed through the combination Γ, that will make either $g_{\pm}$ the critical composition at threshold. For strongly phase separating systems, such as $LiFePO_4$, we find asymptotic approximations of the solutions of (52) in the small parameter $1/\tilde{a}$. Two term expansions for each root are

$$g_1 \sim e^{-2\tilde{a}/3}\left(\frac{1}{\Gamma^{2/3}}+\frac{4\tilde{a}\,e^{-2\tilde{a}/3}}{3\Gamma^{4/3}}\right), \tag{54}$$

$$g_2 \sim \frac{1}{2}-\frac{1}{2}\ln\left(\frac{\sqrt{2}}{\Gamma}\right)\left[\frac{1}{\tilde{a}}+\frac{5}{2\tilde{a}^2}\right], \tag{55}$$

$$g_3 \sim 1-e^{-\tilde{a}}\left(\Gamma+2\tilde{a}\Gamma^2\,e^{-\tilde{a}}\right). \tag{56}$$

The existence of traveling waves and the selection of the wave velocity in a phase separated system can be understood by a linear stability analysis of (49) and (50) about the three stationary points $(g_i,0)$ for $i=1,2,3$. We find that $(g_1,0)$ and $(g_3,0)$ are saddle points for all velocities, and $(g_2,0)$ is either a stable node or stable spiral, depending on the velocity. Monotonic wavefronts between the equilibrium Li-poor and Li-rich phases correspond to trajectories in the (g,h) phase space that connect $(g_1,0)$ and $(g_3,0)$, bypassing $(g_2,0)$. Following the continuity arguments presented in [39], there is a unique velocity v such that the orientation of the eigenvectors at $(g_1,0)$ and $(g_3,0)$ allow a single trajectory joining these points. Thus, for a given set of parameters, all fully developed waves in a system propagate at the same velocity.

A rigorous mathematical analysis of the traveling-wave solutions of (27), including their formal existence, stability, and velocity is beyond the scope of this work. Although analytical methods for studying traveling waves in parabolic systems are available [40], they are usually developed for systems where there is a diffusion term plus a source independent of derivatives of the solution, as in (33). To the best of our knowledge, (27) represents a different type of equation admitting traveling-wave solutions, where the curvature dependence of the source precludes the need for an explicit diffusion term.

The nanoscale dimensions of the physical domain also complicate the analysis of (27). In other reaction diffusion equations, such as the Fisher equation, the wave velocity is determined by assuming an exponential decay of the leading edge of the wavefront as $\tilde{x}\to\infty$ [39]. A finite cutoff in the leading edge is known to significantly alter the velocity [41]. Such cutoffs are present in nanoparticles of $LiFePO_4$, as the xz surface is bounded on the scale of the wave width. Moreover, the nanometer wave width describes the Li concentration across only a few atomic layers of the crystal, with each 1D channel in the layer holding a single file of Li atoms. Therefore, $\bar{c}$ may be discontinuous for small particles.

In spite of these difficulties, we close by predicting bounds on the external chemical potential required for the existence of SRL waves in our model. As discussed in the main text, large chemical potentials exceeding these bounds increase surface reactions to the point where bulk transport becomes rate limiting. The extreme negative and positive values of $\tilde{\mu}_e$ in Fig. 7 represent these bounds in the numerical simulations; there are no traveling wave solutions beyond them.

The bounding values of $\tilde{\mu}_e$ can be determined analytically by solving (52) for the $\tilde{\mu}_e^{\mp}$ corresponding to the extrema $g_{\pm}$ given by

(53), as these compositions define the limits of the phase separation range. We obtain

$$\tilde{\mu}_e^{\mp} = \tilde{a}(1-2g_{\pm}) + \ln\left(\frac{g_{\pm}^{3/2}}{1-g_{\pm}}\right) + \ln\sqrt{\kappa}, \quad (57)$$

where $\tilde{\mu}_e^{-}$ is the minimum allowable potential for extraction waves, and $\tilde{\mu}_e^{+}$ is the maximum allowable potential for insertion waves. The notational $\pm$ signs of $g_{\pm}$ and $\tilde{\mu}_e^{\mp}$ are reversed since g_{-} is the minimum extremum at which there is almost only insertion, hence corresponding to the maximum allowable potential $\tilde{\mu}_e^{+}$, and conversely for g_{+} and $\tilde{\mu}_e^{-}$.

References

[1] A.K. Padhi, K.S. Nanjundaswamy, J.B. Goodenough, J. Electrochem. Soc. 144 (1997) 1188.
[2] A. Yamada, S.C. Chung, K. Hinokuma, J. Electrochem. Soc. 148 (2001) A224.
[3] S.Y. Chung, J.T. Bloking, Y.M. Chiang, Nat. Mater. 1 (2002) 123.
[4] C. Delacourt, P. Poizot, J.M. Tarascon, C. Masquelier, Nat. Mater. 4 (2005) 254.
[5] V. Srinivasan, J. Newman, J. Electrochem. Soc. 151 (2004) A1517.
[6] M. Doyle, T.F. Fuller, J. Newman, J. Electrochem. Soc. 140 (1993) 1526.
[7] D. Morgan, A.V. der Ven, G. Ceder, Electrochem. Solid State Lett. 7 (2004) A30.
[8] C.Y. Ouyang, S.Q. Shi, Z.X. Wang, X.J. Huang, L.Q. Chen, Phys. Rev. B 69 (2004) 104303.
[9] M.S. Islam, D.J. Driscoll, C.A.J. Fisher, P.R. Slater, Chem. Mater. 17 (2005) 5085.
[10] F. Zhou, T. Maxisch, G. Ceder, Phys. Rev. Lett. 97 (2006) 155704.
[11] T. Maxisch, G. Ceder, Phys. Rev. B 73 (2006) 174112.
[12] Y.N. Xu, S.Y. Chung, J.T. Bloking, Y.M. Chiang, W.Y. Ching, Electrochem. Solid State Lett. 7 (2004) A131.
[13] F. Zhou, K.S. Kang, T. Maxisch, G. Ceder, D. Morgan, Solid State Commun. 132 (2004) 181.
[14] T. Maxisch, F. Zhou, G. Ceder, Phys. Rev. B 73 (2006) 104301.
[15] G.Y. Chen, X.Y. Song, T.J. Richardson, Electrochem. Solid State Lett. 9 (2006) A295.
[16] L. Laffont, C. Delacourt, P. Gibot, M.Y. Wu, P. Kooyman, C. Masquelier, J.M. Tarascon, Chem. Mater. 18 (2006) 5520.
[17] R. Amin, P. Balaya, J. Maier, Electrochem. Solid State Lett. 10 (2007) A13.
[18] N. Meethong, H.Y.S. Huang, S.A. Speakman, W.C. Carter, Y.M. Chiang, Adv. Funct. Mater. 17 (2007) 1115.
[19] B.C. Han, A.V. der Ven, D. Morgan, G. Ceder, Electrochim. Acta 49 (2004) 4691.
[20] M.E.A. y de Dompablo, A.V. der Ven, G. Ceder, Phys. Rev. B 66 (2002) 064112.
[21] A.V. der Ven, G. Ceder, Electrochem. Commun. 6 (2004) 1045.
[22] J.W. Cahn, J.E. Hilliard, J. Chem. Phys. 28 (1958) 258.
[23] K. Thornton, J. Agren, P.W. Voorhees, Acta Mater. 51 (2003) 5675.
[24] A.G. Khachaturyan, Theory of Structural Transformations in Solids, Wiley–Interscience, New York, 1983.
[25] F.C. Larche, J.W. Cahn, Acta. Meter. 33 (1985) 331.
[26] A.V. der Ven, G. Ceder, Electrochem. Solid State Lett. 3 (2000) 301.
[27] J.O. Bockris, A.K.N. Reddy, Modern Electrochemistry, Plenum, New York, 1970.
[28] J. Newman, Electrochemical Systems, 2nd ed., Prentice-Hall Inc., Englewood Cliffs, NJ, 1991.
[29] L. Wang, F. Zhou, Y.S. Meng, G. Ceder, Phys. Rev. B 76 (2007), art. no. 165435.
[30] M. Z. Bazant, D. Lacoste, K. Sekimoto, in preparation.
[31] S.F. Yang, J. Power Sources 119 (2003) 239.
[32] G.I. Barenblatt, Scaling, Self-similarity, and Intermediate Asymptotics, 2nd ed., Cambridge University Press, 1996.
[33] C.J. Wen, B.A. Boukamp, R.A. Huggins, W. Weppner, J. Electrochem. Soc. 126 (1979) 2258.
[34] R.W. Ballufi, S.M. Allen, W.C. Carter, Kinetics of Materials, John Wiley & Sons., Hoboken, NJ, 2005.
[35] M. Gaberscek, M. Kuzma, J. Jamnik, Phys. Chem. Chem. Phys. 9 (2007) 1815.
[36] J.L. Allen, T.R. Jow, J. Wolfenstine, Chem. Mater. 19 (2007) 2108.
[37] N. Ravet, Y. Chouinard, J.F. Magnan, S. Besner, M. Gauthier, M. Armand, J. Power Sources 97 (8) (2001) 503.
[38] P.S. Herle, B. Ellis, N. Coombs, L.F. Nazar, Nat. Mater. 3 (2004) 147.
[39] J.D. Murray, Mathematical Biology I, Springer-Verlag, New York, 2002.
[40] A.I. Volpert, V.A. Volpert, V.A. Volpert, Traveling Wave Solutions of Parabolic Systems, American Mathematical Society, Providence, RI, 1994.
[41] E. Brunet, B. Derrida, Phys. Rev. E 56 (1997) 2597.